Spectral approach to electron emission analysis from heterogenous surfaces

Jonathan Ludwick, Guilhem Saïz, Ludovic Douillard, Tyson Back, Ali Sayir

A Spectral Approach to Electron Emission Analysis from Heterogenous Surfaces

J. Ludwick[1,2], G. Saiz[3], L. Douillard[3], T.C. Back[1*], *and* A. Sayir[4]

[1] Materials and Manufacturing Directorate, Air Force Research Laboratory, Wright-Patterson Air Force Base, Ohio 45433, USA
[2] UES, a BlueHalo company, 4401 Dayton-Xenia Rd, Dayton, OH 45432
[3] Université Paris-Saclay, CEA, CNRS, SPEC, F-91190 Gif sur Yvette, France
[4] Air Force Office of Scientific Research, Arlington, VI, USA
*Corresponding Author

Abstract

This study introduces a methodology to extract multi-work function distributions directly from Thermally Emitted Electron Distribution (ThEED) data, addressing the limitations of traditional Richardson-Laue-Dushman methods for heterogeneous thermal emission cathodes. The approach involves deconvolving measured Thermally Emitted Electron Distributions with an instrument response function (derived from a homogeneous sample) and then applying a steepest-descent algorithm to determine the relative contributions of various work functions, while also considering the impact of external electrostatic fields on patch field effects. The methodology is validated using single-phase Mayenite $[Ca_{24}Al_{28}O_{64}]^{4+}(4e^{-})$, an electride material with spatially varying work functions, by comparing the predicted distributions with Photoemission Electron Microscopy (PEEM) work function maps and Monte Carlo simulations. Results demonstrate excellent agreement between the predicted and measured work function distributions, highlighting the method's accuracy in resolving surface heterogeneity. Furthermore, the technique is successfully applied to ThEED data taken at a characterized surface location, showing promise for analyzing complex emission patterns in thermal emission cathodes. This methodology eliminates the need for complementary, potentially spatially mismatched, surface characterization techniques, offering a powerful tool for understanding and designing advanced thermal emitters.

INTRODUCTION

Many modern thermal emission cathodes, including electrides and dispenser cathodes, are characterized by complex microstructures, which are clearly delineated on their surfaces. The spatial heterogeneity of these emitters creates complex emission patterns that are not well defined by the Richardson-Laue-Dushman (RLD) equation of thermal emission electron current density against temperature [1,2]. Emitters with heterogeneous surface structures incur phenomena such as spatially varying emission intensity, non-uniform space charge, and patch field effects [3–5]. Accurate correlation of electron emission characteristics with the underlying surface microstructure and work function is essential for optimizing emitter performance. Therefore, a thermal emission analysis technique capable of directly determining these surface properties from thermal emission measurements is required. This approach circumvents the spatial mismatch and potential inconsistencies inherent in using separate characterization methods [5] and is crucial for enabling data-driven emitter design improvements.

In this study, we propose a method to predict a work function distribution on a heterogeneous surface using a measured Thermally Emitted Electron Distribution (ThEED). Although this work focuses on thermal emission, the developed methodology provides a framework that can be adapted to analyze field emission energy distributions. The observed energy distribution in a ThEED closely relates a Fermi-Dirac distribution characteristic of the material's electronic states but is modulated by the energy-dependent emission probability and is broadened due to the analyzer resolution. For polycrystalline surfaces, the ThEED spectrum may be more complex than phase pure or single crystals, exhibiting multiple features or a broadened cutoff characteristic, and we will discuss how these features can be used to infer information about surface heterogeneity. To assist in validating the work function distributions extracted from the ThEEDs, we employed Photoemission Electron Microscopy (PEEM). This technique offers a versatile approach for mapping the work function with high spatial resolution, enabling real-time imaging, providing surface sensitivity, and facilitating quantitative measurements. The resulting PEEM images can be directly correlated with the sample's surface heterogeneity. Utilizing single-phase Mayenite, an electride material that comprises grains with variable work function, we present a methodology for determining the work function distribution across a crystalline surface through analysis of ThEED curves. Mayenite ($12CaO \bullet 7Al_2O_3$), commonly denoted as C12A7, is a promising material for thermal emission cathodes. Its stoichiometric composition is characterized by the formula $[Ca_{24}Al_{28}O_{64}]^{4+}(O^{2-})_2$, where oxygen ions are encapsulated within the aluminate framework's cage structures. Of particular interest for thermal emission applications is its electride derivative, C12A7:e^-. In C12A7:e^-, these encapsulated oxygen ions are replaced by an equivalent charge of delocalized electrons, leading to the chemical formula $[Ca_{24}Al_{28}O_{64}]^{4+}(4e^-)$. This anionic substitution results in a significantly reduced work function and metallic transport properties, which are highly desirable for efficient electron emission. For clarity within this study, C12A7 will refer to the pure Mayenite, and C12A7:e^- to its electride form.

Researchers have explored various methods to create stable, crystalline Mayenite, including thin film deposition, melt processing, single crystal growth, and a range of post-processing treatments involving anions (like OH^-, O^{2-}, O^-, Cl^-, F^-, and H^-) and calcium metal. Kim *et al.* [6] provide an

overview of these techniques. In prior studies [7,8], a fabrication method employing carbon dimer (C_2^-) ion templating within the $[Ca_{24}Al_{28}O_{64}]^{4+}$ framework resulted in materials exhibiting a range of work function values. This process culminated in the production of a C12A7:e^- electride with an exceptionally low work function of 0.9 eV. Significantly, this electride exhibited electron emission at relatively low temperatures, commencing at 650 °C [7]. The observed low work function and metallic transport characteristics are attributed to the formation of a cage-based conduction band within the electride structure. This is significant for two reasons: first, the energy required to liberate an electron from the C12A7:e^- framework is exceptionally low compared to many metals. Second, C12A7:e^- is a robust oxide electride, exhibiting electron emission properties across a broad spectrum of harsh conditions [9], including iodine- or oxygen-rich atmospheres, reducing environments, and vacuum, up to 1100 °C. Notwithstanding these exceptional characteristics, the observed discrepancies in work function values of Mayenite determined using the Richardson-Dushman equation necessitate further investigation and serve as the primary motivation for this study. Previous investigations have largely focused on the macroscopic response of Mayenite, yielding average electron emission characteristics without resolving the spatial distribution of electron emission sites across the surface.

EXPERIMENTAL

Synthesis was achieved within a graphite resistance-heated furnace for all samples, where the temperature was ramped at a rate of 20 °C/min to a dwell temperature between 1300 °C and 1400 °C and subsequently maintained for 1 to 16 hours. Subsequently, the furnace was cooled to room temperature at a rate of 20 °C/min. The furnace atmosphere consisted of either flowing helium or a dynamic rough vacuum (approximately -30 mm in Hg gauge). To verify phase purity, the synthesized materials were ground into a fine powder using a mortar and pestle. The crystal structure and phase composition were then characterized by X-ray diffraction (XRD) using a Bruker D-8 Advance diffractometer (Billerica, MA) with Cu Kα radiation in the Bragg-Brentano geometry. XRD patterns were acquired over a 2θ range of 10° to 80° with a scan rate of 3.5 °/min, employing 4° Soller slits. A more detailed account of the sample preparation details are described elsewhere [7].

ThEED measurements characterize the kinetic energy distribution of emitted electrons using an electron energy spectrometer. Depending on the analyzer setup, the kinetic energies can represent only the component normal to the emitting surface or the total kinetic energy. ThEED measurements were taken using a Scienta Omicron Argus CU multipurpose analyzer as illustrated in Figure 1. A hemispherical energy analyzer was used to observe the total energy component of the electron kinetic energies. A measurement on this system will return a spectrum of electron counts per second per unit energy range. This spectrum is built by sequentially scanning one energy at time and recording electron counts per second. Multiplying this measured spectrum by the elementary charge e (positive magnitude in emission physics) then dividing by the analysis area of ~0.0034 mm^2 returns the ThEED in units of electron current density per unit energy range henceforth denoted as j_{obs}.

The backside of the sample was heated via a Pyrolithic Boron Nitride (PBN) heater. A Keithley 6517a multimeter kept the sample at a constant -300 V to accelerate low energy thermally emitted electrons into the analyzer. The electrostatic (ES) field magnitude between the sample and analyzer was $10\ kV/m$. An optical pyrometer was positioned on the sample surface to get an accurate readout of the temperature at the emitting region. The C12A7:e^- sample, with a black color, was assumed to have an emissivity of 0.9 [10,11].

The instrument aperture defined a circular analysis area of 66 μm diameter on the sample surface. This is treated as the effective area for electron emission. A constant pass energy of 5 eV was used for all measurements. The sample was initially heated to a controlled temperature of 1000 K for 90 minutes for conditioning. A conditioning period was implemented to ensure stable and consistent electron emission from the sample. Upon reaching the maximum target temperature, the detector count rate exhibited a monotonic increase as a function of time. Following 90 minutes of isothermal heating at the maximum temperature, the emission rate asymptotically approached a near-equilibrium value. Subsequently, the sample temperature was gradually reduced to decrease the emitted electron flux. Cooling continued until the detector count rate reached a safe level ($\leq$ 4 million counts per second), preventing potential damage to the detector. ThEED scans were then setup to have a window of 302 to 304.2 eV with the ThEED peak to be near the center. 0.01 eV energy steps were taken, each with a 0.05 second dwell time. Each ThEED measurement took approximately 19 seconds, including analyzer software delays. ThEED scans were acquired repeatedly during slow cooling of the sample at a rate of approximately $1\ K$ every 14 seconds. This cooling rate was selected to minimize temperature variations during each scan, approximating isothermal conditions across the measured energy range. The pyrometer reading at the conclusion of each scan was assumed to represent the constant sample temperature throughout that scan.

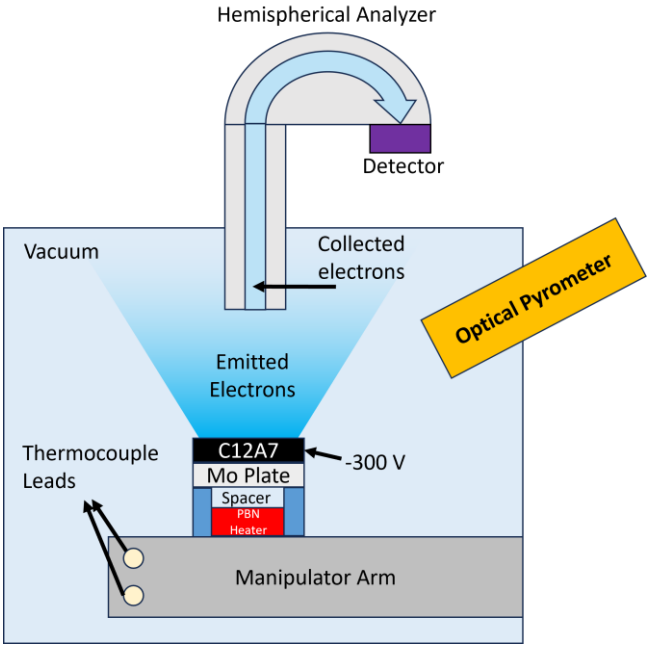

Figure 1: Experimental setup for measuring thermal electron emission energy distributions.

ThEED measurements characterize the kinetic energy distribution of emitted electrons by using an electron energy spectrometer. Depending on the geometry of the emitter + analyzer system, and possibly on the value of the extraction field, the measurements can in principle relate either to the distribution of electron total-energy at the point of emission from the emitter surface (the TED), or to the distribution of the energy component that is normal to the emitter surface at the point of emission (the NED), or to something intermediate. The experimental setup shown in Figure 1 observes a TED in the context of thermal emission, see the appendix for more details.

In accordance with the electron emission convention, this work treats electron currents and their corresponding densities as positive values, contrary to their negative assignment in conventional electrical theory.

Photoemission electron microscopy (PEEM) was conducted using a Scienta Omicron nanoESCA energy-filtering photoemission microscope. A FOCUS mercury arc UV source illuminated the sample with a 5.2 eV photon energy. Real-space PEEM images with a field of view of about 70 μm were taken scanning photo-emitted electron kinetic energies from 0 to 5.2 eV with 0.01 eV steps. This measurement results in a three-dimensional data matrix (data cube) with a stack of 521 PEEM images, each consisting of 1024 x 1024 spatially resolved intensity values across the sample surface. Hereafter, the variation of photoelectron emission intensity as a function of energy from a single point on the sample surface will be referred to as the photoelectron emission distribution (PhEED). Spatially resolved work function maps can then be extracted from the data cube by doing a pixel-by-pixel analysis which consists of fitting a complementary error function [13] to each of the 1024 x 1024 PhEEDs. This fitting method takes the inflection point of the intensity onset to be the work function. Fitting complementary error functions to the 1024 x

1024 PhEED data cube is computationally demanding. To circumvent this, first a frequency filter was applied along the energy axis to reduce measurement noise. Then, a numerical derivative was applied to each PhEED to find the inflection point. This derivative-based method demonstrated a significant reduction in computational time compared to complementary error function fitting. To illustrate the efficacy of this approach, Figure 2 presents a comparative analysis of work function extraction using both the complementary error function fitting and the derivative-based methods. This comparison was performed on a selected PhEED spectrum from the data cube. The derivative method yielded a work function value of 3.20 eV, while the complementary error function fitting method resulted in a value of 3.19 eV. The close agreement between these values indicates that the derivative method provides a comparable level of accuracy to the more computationally intensive error function fitting technique.

When collecting a PhEED, the energy resolution of the detector will determine some finite amount of spatial energy dispersion in the vertical direction [14,15]. This dispersion is compensated for in post-processing by finding a homogenous region of the surface and collecting a work function map. The parabolic change of measured work function in the dispersion direction is then subtracted from future work function maps to eliminate dispersion effects.

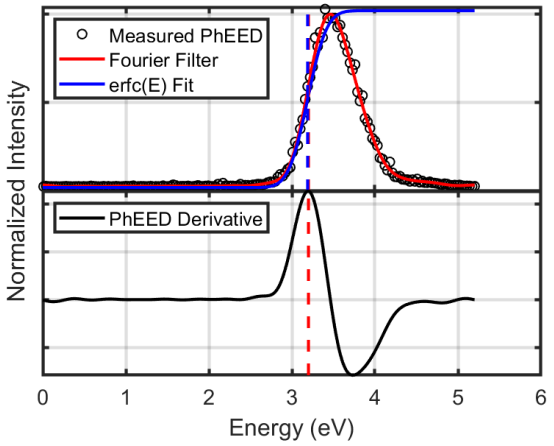

Figure 2: (Top) Measured PhEED, frequency filtered PhEED, and complimentary error function fit shown by the black circles, red curve, and blue curve, respectively. Vertical dashed lines represent the extracted work functions using the derivative and complimentary error function methods, with red and blue lines, respectively. (Bottom) Numerical PhEED energy derivative after applying a frequency filter. Maximum of this curve (represented by vertical red line) represents the inflection point of the PhEED and therefore the work function. All curves are normalized to their peak intensity.

RESULTS

For the computational analysis, ThEED's can be determined as either normal energy distributions (NEDs) or total energy distributions (TEDs) depending on the analyzer [16]. A NED only accounts for the initial normal energy of an electron as it emits from a sample, while a TED

accounts for the initial total energy (sum of normal and transverse components) of the emitted electron. Additionally, an analyzer designed for measuring NEDs may inadvertently measure a TED if the emitter is hemispherical in shape. Careful distinction between NEDs and TEDs must be made before properly characterizing a ThEED.

A typical ThEED in units of electron current density per unit energy range can be described mathematically by:

$$j_n(\mathrm{T}, E_n) = z_s k_B T exp\left(-\frac{E_n}{k_B T}\right) H(E_n - \phi),$$
$$j_{tot}(\mathrm{T}, E_{tot}) = z_s (E_{tot} - \phi) \exp\left(-\frac{E_{tot}}{k_B T}\right) H(E_{tot} - \phi), \quad (1)$$

with the Sommerfeld electron supply constant z_s represented as

$$z_s = \frac{4\pi em}{h^3} \approx 1.618311 \times 10^{14}\ A\ m^{-2}\ eV^{-2}, \quad (2)$$

where $j_n(\mathrm{T}, E_n)$ is the ThEED of normal energies [17,18], $j_{tot}(\mathrm{T}, E_{tot})$ is the ThEED of total energies [19]. These represent electron current density per unit normal energy and total energy range, respectively. E_n and E_{tot} are the energies at the point of emission of thermally emitted electron normal and total energy components, respectively, in reference to the Fermi level. The electron mass is m, the charge magnitude of an electron denoted as e, a positive quantity in emission physics. $\hbar$ is the reduced Planck's constant, k_B is the Boltzmann constant, ϕ is the sample work function, and $H(E_n - \phi)$ is the Heaviside step function. The methodology for work function extraction is the same regardless if analyzer observes E_n or E_{tot}. The electron energy will henceforth be denoted as E representing an interchangeable term for either energy type. In the case of the experiments of this work, $\boldsymbol{E_{tot}}$ was observed.

There is a strong difference in shape between j_n and j_{tot} as shown in Figure 3. In the case of thermal emission, j_n will be much narrower than j_{tot} with a peak directly at the onset of emission. However, the inherent instrumental broadening of the analyzer, stemming from its finite resolution, necessitates the convolution of the intrinsic theoretical functions with the instrument's response function. This process broadens the observed peak of j_n and can shift its apparent maximum relative to the true emission onset. This broadening effect is discussed in more detail in the next section.

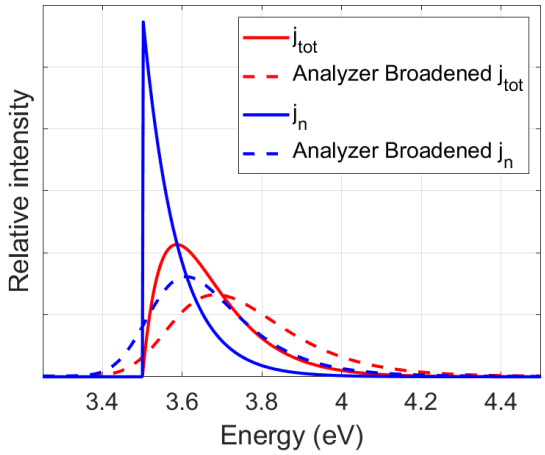

Figure 3: Comparison of a typical NED and TED from j_n and j_{tot}, respectively, in Eq. (1) shown by the solid curves. The dashed curves show an emulated analyzer broadening effect at a pass energy of 5 eV on both j_n and j_{tot} demonstrating how different a real measurement may appear than Eq. (1).

By fitting an appropriate ThEED with the form of Eq. (1), one can extract the work function of the sample emission site if the temperature is known. However, there are three important considerations to take into account before applying this fit: (1) the energy distribution analyzer will smear the ThEED pattern, (2) C12A7:e^- electride samples were polycrystalline and had variations in surface termination and crystallographic orientation across the analysis area of individual grains, which inherently possess different electron affinities, and (3) surface patch fields, originating from local work function variations, distort emitted electron energies and trajectories in ThEED measurements. This leads to broadening, shifting, or other distortions in the measured ThEED, preventing it from accurately reflecting the true work function distribution and thus yielding an apparent, rather than intrinsic, work function profile.

Instrumental Resolution Function, originating from the finite resolution of the energy analyzer, fundamentally impacts the accurate interpretation of acquired energy spectra. Knowledge of the analyzer's contribution to the broadening of ThEED patterns is necessary for accurate deconvolution and extraction of intrinsic material properties. The analyzer's instrumental resolution function ($IRF(\Delta E)$), where ΔE is the energy offset, represents the probability distribution of the analyzer's response to a perfectly monoenergetic source**.** Once $IRF(\Delta E)$ is characterized, quantitative parameters such as work function and sample temperature can be accurately extracted from ThEED spectra. This can be done using Lucy–Richardson deconvolution [20,21], an iterative procedure used to recover a signal blurred by a point spread function. In this case, deconvolution is applied to derive the point spread function (PSF) representing the analyzer broadening, by comparing the measured ThEED with the theoretical ThEED obtained from Eq. (1). In this work, the MATLAB function "deconvlucy" in the Image Processing Toolbox for image deconvolution employing the Lucy-Richardson algorithm was used with 100 iterations. Other groups have approximated $IRF(\Delta E)$ using a Gaussian function [22,23] which can be a much simpler approach. If it is assumed $IRF(\Delta E)$ is Gaussian, an error function can be fit to the leading edge of ThEED data, and the derivative of the error function will result in a Gaussian that can be

used as a quick approximation of $IRF(\Delta E)$. However, Reifenberger et al. show $IRF(\Delta E)$ can be inherently asymmetrical due to field penetration effects in a retarding grid [24], and proposed a direct method using experimental data. This method involves conducting a Fourier transform on measured data and dividing out Eq. (1). An issue that arises with this method is that noise can be significantly amplified in this process, so the authors inject an artificial Gaussian mask introducing error into the shape of $IRF(\Delta E)$. In this study, the Lucy–Richardson deconvolution method was identified as the most suitable for the reconstruction of $IRF(\Delta E)$, owing to its inherent robustness and directness. Once obtained, $IRF(\Delta E)$ can be used for deconvolution of broadening in any future ThEED data, even if the analysis area consists of multiple work functions. However, the successful application of this method is contingent upon satisfying several critical prerequisites. Non-compliance with these conditions will compromise the accuracy of the derived $IRF(\Delta E)$ and propagate errors throughout the subsequent ThEED analysis.

Specifically:

- **Work Function Homogeneity:** The deconvolution to derive $IRF(\Delta E)$ must be performed on a sample region exhibiting a uniform work function. This homogeneity is crucial, as Eq. (1) inherently assumes a singular work function for accurate modeling,
- **Precise Temperature Knowledge:** Accurate knowledge of the sample temperature at the point of analysis is required to correctly account for the temperature-dependent spectral shape of the theoretical ThEED as described by Eq. (1),
- **Measurement Noise Minimization:** Minimization of measurement noise is paramount, as excessive noise levels can be amplified by the deconvolution process, thereby introducing artifacts and compromising the fidelity of the derived $IRF(\Delta E)$,
- **Consistent Analyzer Resolution Settings:** The analyzer's energy resolution settings (e.g., pass energy and slit width) must be meticulously maintained for any subsequent measurements utilizing the derived $IRF(\Delta E)$. Variations in these settings will alter the instrument's broadening function, invalidating the previously extracted $IRF(\Delta E)$ for comparative analysis.

Multiple work functions in the sample analysis area would not be properly represented by Eq. (1), as this function only assumes a single work function. The temperature must be known to adjust the shape of the expected ThEED in Eq. (1). Measurement noise could introduce error into $IRF(\Delta E)$.

Distribution Work function Values necessitated additional considerations for real cases, such as working with a sample consisting of multiple work functions across the analysis area. In these cases, the measured ThEED curve will broaden as more work functions are introduced, making quantitative analysis difficult. If all the work functions and their corresponding emission contributions were known, a ThEED curve, in units of electron current density per unit energy range, could be generated by summing together a scaled instance of Eq. (1) for each work function,

$$\mathrm{j}_{sum}(E) = \sum_{x=1}^{N} A_x \, \mathrm{j}_x(E, \phi_x) \qquad (3)$$

where $\mathrm{j}_{sum}(E)$ is the total ThEED, $\mathrm{j}_x(E, \phi_x)$ is the ThEED for an individual work function ϕ_x, and A_x is the scaling factor for the emission contribution of each work function. Physically, a normalized A_x represents the percent of the analysis surface area that particular work function makes up. Convolution of $\mathrm{j}_{sum}(E)$ and $IRF(\Delta\mathrm{E})$ can then be performed to reconstruct the experimentally measured energy distribution ($\mathrm{j}_{obs}(E)$).

However, in the case that work function distribution across the analysis area is unknown, the distribution can be numerically determined via a steepest descent algorithm. This method is an iterative algorithm taking steps in the direction of the greatest negative slope to find a minimum in N-dimensional space. In this case, the minimum being sought after is a fitting error matching the convolution of $IRF(\Delta\mathrm{E})$ and j_{sum} to j_{obs}. A distribution of evenly spaced work functions needs to be established across relevant energies to encompass the entire ThEED. The number of chosen work functions must be large enough to accurately resolve the work function distribution, but small enough for the algorithm to complete within a reasonable time depending on available computational resources (this work used 50 evenly spaced work functions with 10 meV steps). Spacing out work functions at 10 meV usually allows fine features in the distribution to emerge. The best minimum work function spacing to use will vary depending on the complexity of the heterogenous surface. It is best to initially space the work functions at 10 meV and then compare the result to a finer spacing result. Keep decreasing spacing until results generate the same general shape of work function distribution.

The value of A_x in Eq. (3) is altered for each work function, one at a time, so that the convolution of $\mathrm{j}_{sum}(E) * IRF(\Delta\mathrm{E})$ yields a good fit to j_{obs}. This is done by numerically analyzing the derivative of the residual standard error (RSE) of the final fit for j_{obs} with respect to each A_x value ($\frac{\partial RSE}{\partial A_x}$). A_x is then stepped in the direction of the negative slope with a step size proportional to the magnitude of $\frac{\partial RSE}{\partial A_x}$. As the correlation between the model and the data increases, $\frac{\partial RSE}{\partial A_x}$ reduces and the A_x step sizes get smaller. This process is iteratively repeated until a desired convergence is reached as shown in Figure 4. The determined values of A_x should be near consistent across different temperatures, with slight variation as material work functions can slightly change with temperature.

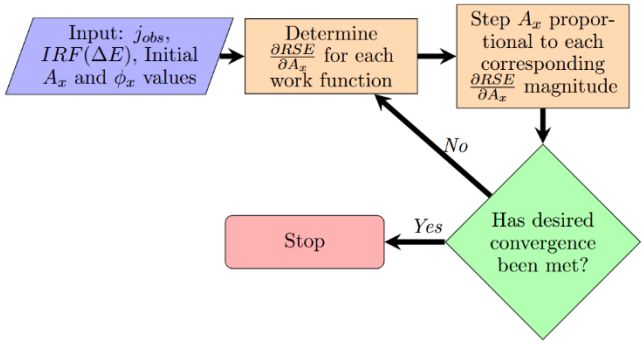

Figure 4: Flow chart for determining work function distribution via the steepest descent algorithm.

Patch fields, as distinct work function regions, are key to understanding the spatially heterogeneous work functions in cathodes, which are also characterized by a mean work function $\overline{\phi_0}$. In the presence of patch fields, the establishment of a common Fermi level throughout the cathode material results in a spatially varying vacuum level across the surface. This variation is directly correlated with the local work function differences between adjacent patches. This situation creates a contact potential between different work function patches to generate an inherent ES field (patch field F_p) near the surface that is present even in the absence of an applied ES field [3,4,25]. Note that following electron emission convention, these ES fields have a negative quantity, but are represented as positive magnitudes. Though this ES field is too weak by itself to produce field or Schottky emission, it can still notably affect thermal emission. The measured work functions in the ThEED (ϕ) may differ from the actual surface work functions ϕ_0. Typically, to collect thermally emitted electrons, a weak external ES field (F_{ext}) below the threshold of Schottky emission is applied ($\sim< 10^3\ kV/m$). When choosing an external ES field, three cases for patch fields can occur. (1) If $F_{ext} << F_p$, patches with $\phi_0 \leq \overline{\phi_0}$ will not show their true work functions in the measurement, as they will appear to thermally emit with an apparent work function $\phi \approx \overline{\phi_0}$. (2) If F_{ext} and F_p are comparable in magnitude, some of the $\phi_0 \leq \overline{\phi_0}$ patches will begin to thermally emit with $\phi < \overline{\phi_0}$, but very small ϕ_0 will still not be observed. (3) If $F_{ext} >> F_p$ without initiating Schottky emission, there will be no difference between ϕ_0 and ϕ allowing measured work functions to match their true values.

Figure 5 shows a randomly generated patch surface with $\overline{\phi_0} = 3.5\ eV$ and a ± 0.5 eV work function variation. Each patch is a 10 X 10 μm^2 square. A size of 10 µm x 10 µm is representative of the grain sizes observed on the surface, see work function maps in Figure 13. Using COMSOL Multiphysics, a Laplace solution was found, assuming an infinite anode plate 100 μm above the patch surface. The determined electric potential along a straight line perpendicular to select patches (at locations marked by a X in Figure 5) shows their corresponding potential energy barriers, as shown in Figure 6. The anode voltage is adjusted to produce an external ES field of 0.1 kV/m, 50 kV/m, and 250 kV/m representing the $F_{ext} << F_p$, $F_{ext} \approx F_p$, and $F_{ext} >> F_p$ cases, respectively. Here, it is assumed that emission only occurs over the barriers, as these barriers are far too wide to allow tunneling. This keeps Eq. (1) relevant across all these emission cases. The highest point on a barrier (regardless of distance) represents the apparent ϕ observed in ThEED. At 250 kV/m, all the patches emit where the apparent work function matches the actual $\phi_0 = \phi$.

A reduction in the external ES field leads to an elevation of the potential energy barrier at the low work function patches, causing the apparent work function (ϕ) to increase and converge towards the spatial average work function $\overline{\phi_0}$. Understanding this disparity between ϕ and ϕ_0 is critical when working with ThEEDs. If the external ES field is too small, low work function patches will not be observed, as their apparent work function ϕ is increased towards the spatially averaged work function $\overline{\phi_0}$. ThEEDs are ultimately a function of external ES field strength until the $F_{ext} >> F_p$ condition is met.

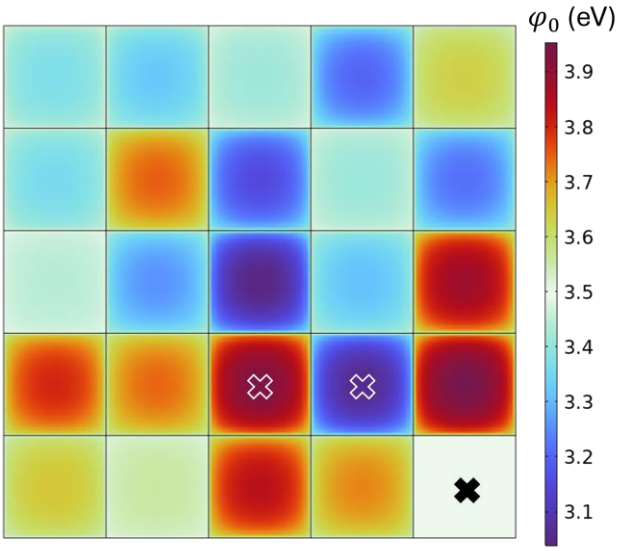

Figure 5: Surface generated with 10 X 10 μm^2 work function patch squares. These work functions were randomized to have $\overline{\phi_0} = 3.5\ eV$ with a ± 0.5 eV variation. The X's mark patches where the potential energy barrier along a straight line perpendicular to the surface is shown in Figure 6. Potential energies are smoothed near square edges to avoid ES field singularities in simulations.

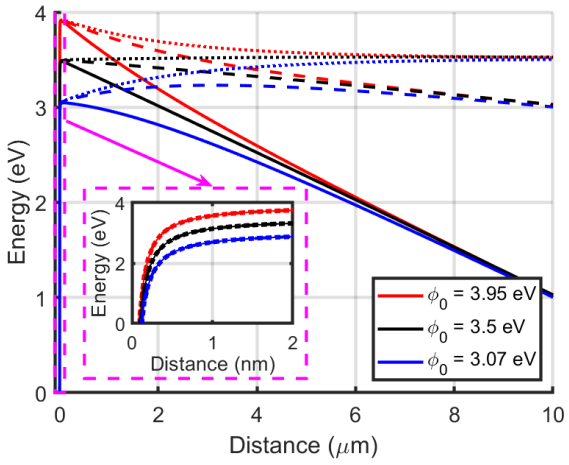

Figure 6: Potential energy barriers for select points on generated surface in Figure 5. The barriers are observed at the exact center of a 3.95 eV (red X), 3.5 eV (black X), and 3.07 eV (blue X) patch represented with blue, black, and red lines, respectively. The dotted, dashed, and solid lines

represent external ES fields of 0.1 kV/m, 50 kV/m, and 250 kV/m, respectively. The inset shows a zoomed in distance region of 0 to 2 nm from the emitter surface. This region is relevant to electron tunneling in field emitters. Here, the potential energy barrier does not bend downwards for any of the external ES fields, indicating that these barriers are far too wide for electron tunneling.

DISCUSSION

To determine analyzer broadening effects, a clean, single work function sample is needed for calibration. Single crystal sample of (100) n-type Nb:$SrTiO_3$ in which the surface was prepared following the procedure by Bachelet [26] was selected for this calibration of the analyzer broadening distribution $S(E)$ via the Lucy–Richardson deconvolution method. The carrier concentration of the Nb:$SrTiO_3$ was estimated to be $1.25 \times 10^{20}\ cm^{-3}$ from the doping level, using the method detailed in reference [27]. SrTiO3 is a well-documented material [26] with a sufficiently low work function to collect ThEED. The onset of the ThEED indicates a work function of 3.35 eV for $SrTiO_3$, which is consistent with previous findings [28–30]. The assumed emissivity was 0.8 [31] for temperature measurements. The convolution of a theoretical ThEED $j_{tot}(E)$ from Eq. (1) with a instrument's resolution function $IRF(\Delta E)$ smears the original features, resulting in an observed spectrum where the precision of the initial energy positions is degraded by the detector's finite energy resolution, characterized by $IRF(\Delta\mathrm{E})$. While the original energy *information* is encoded in the resulting distribution, its *sharpness* is lost. $IRF(\Delta\mathrm{E})$ is assumed to be invariant and is employed as a calibration standard for subsequent measurements performed with the same analyzer resolution settings. The invariance of $IRF(\Delta\mathrm{E})$ must be critically evaluated due to potential systematic errors introduced by analyzer instability and the inherent limitations of assuming a constant spectral response.

Figure 7a shows $IRF(\Delta\mathrm{E})$ determined from the $SrTiO_3$ calibration sample and $j_{tot}(E)$ determined using the 3.35 eV work function of STO and temperature of 1062 K. Figure 7b compares the measured ThEED, $j_{obs}(E)$, between 2.8 and 5 eV at a pyrometer temperature of $1062\ K$ to a fit of this measurement from the convolution of $IRF(\Delta\mathrm{E})$ and $j_{tot}(E)$. $j_{obs}(E)$ and its fit nearly perfectly overlapped, indicating $IRF(\Delta\mathrm{E})$ was properly extracted. The energy position of the $IRF(\Delta\mathrm{E})$ peak is not physical and is arbitrarily placed on the energy scale for viewing purposes. Convolution of $IRF(\Delta\mathrm{E})$ with $j_{tot}(E)$ makes the energy position of $IRF(\Delta\mathrm{E})$ irrelevant.

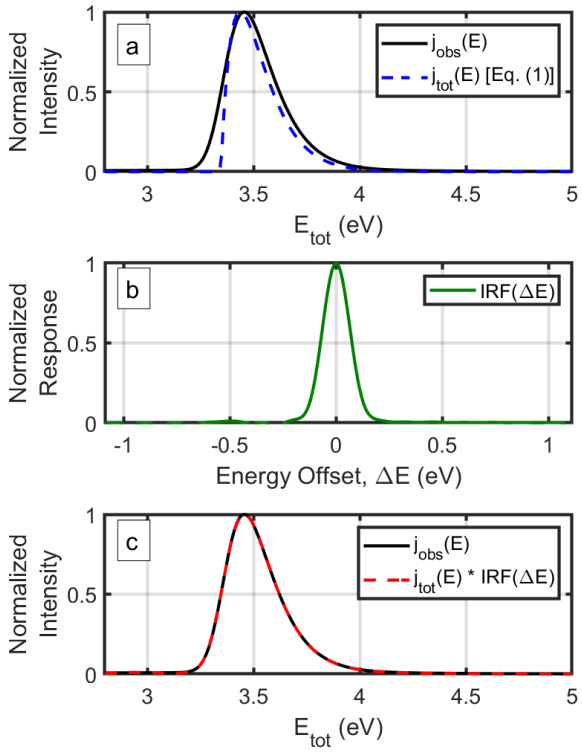

*Figure 7: Figure **a** shows the theoretical $j_{tot}(E)$ distribution from Eq. (1) and the measured $j_{obs}(E)$ distribution with the dashed and solid curve, respectively. To generate the $j_{tot}(E)$ distribution, a measured temperature and work function of $1062\ K$ and $3.35\ eV$ was used, respectively. Due to instrumental resolution constraints, the measured curve was not reproduced. Figure **b** shows the instrumental resolution function $IRF(\Delta E)$. Figure **c** shows the resulting distribution achieved by convolution of the $j_{tot}(E)$ * $IRF(\Delta E)$ distributions against the measured $j_{obs}(E)$ distribution with a dashed and solid curve, respectively. After considering the instrument resolution, the measured curve was nearly perfectly recreated. All spectra are normalized to their peak intensity.*

Figure 8 shows measured ThEEDs of C12A7:e$^-$ normalized by their intensity maxima as temperature is increased. A vertical offset has been applied to each curve to prevent overlapping and facilitate visual comparison. The dashed lines represent high precision fits generated with $j_{sum}(E) * IRF(\Delta E)$. Each curve has a separately determined $j_{sum}(E)$ using the method described in Figure 4. The distribution shows two clear peaks. At low temperatures, the lower energy peak exhibits a relatively higher intensity. However, as the temperature increases, the spectral weight shifts towards the higher energy peak, which becomes the dominant feature. This is in accordance with the following relation:

$$\frac{dj(T, E_n)}{dT} = \frac{k_B T + E_n}{k_B T^2} j(T, E_n), \qquad (4)$$

$$\frac{dj(\mathrm{T}, E_{tot})}{dT} = \frac{E_{tot}}{k_B T^2} j(\mathrm{T}, E_{tot}).$$

For both $j(\mathrm{T}, E_n)$ and $j(\mathrm{T}, E_{tot})$, the rate of intensity change with temperature increases with larger E. If for example, a small area low work function patch (patch A) and large area high work function patch (patch B) were simultaneously emitting at low temperature, patch A, though physically smaller, will dominate emission. As temperature rises, eventually patch B will begin to dominate emission. This trend can only be seen in the presence of multiple work function patches. For the instance of a homogenous single work function surface, the low energy maximum of the ThEED will not be overtaken by a new peak. The dominant peak shifting to a higher energy point in the spectrum is indicative of multiple work functions present, each exhibiting the trend seen in Eq. (4).

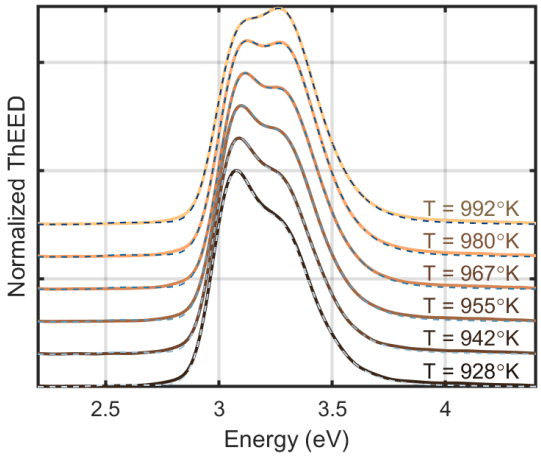

Figure 8: Measured normalized and offset ThEED curves of C12A7:e⁻ at various temperatures shown by solid lines. Dashed lines represent fits generated with $j_{sum}(E) * S(E)$. A unique $j_{sum}(E)$ was generated for each curve. All spectra are normalized to their peak intensity.

Figure 9 (top) shows a contour of normalized ThEED distributions over temperature. The data indicates that the intensity of the high energy peak increases more rapidly with temperature than the intensity of the low energy peak, eventually exceeding it, a trend also evident in Figure 8. Figure 9 (bottom) shows a contour of the extracted work function presence using the steepest descent method outlined in Figure 4. A separate work function distribution was determined at each temperature. The work function values are slightly lower in energy than the ThEED peaks as the ThEEDs are broadened by $S(E)$ and the work function inherently lags the ThEED peak for TEDs, as shown in Figure 3. This offset will increase as analyzer resolution decreases. There are two dominant ThEED peaks representing emission from two distinct work function patches. Additional lower work function patches may exist but are not observable in the ThEED due to an extraction voltage of insufficient magnitude to overcome patch fields that can range from 10s to 100s kV/m depending on patch size. Though the two ThEED peaks are close in magnitude, the work function presence of the two corresponding patches differ greatly. This is due to the low work function patch contributing much more to emission. To have these patches contribute

comparable emission, the areal coverage of the low work function patch in the analysis region must be substantially smaller than the high work function patch. Another interesting note is that the ThEED peaks are 0.15 eV apart while the work function patches are separated by 0.25 eV. This inconsistency arises from the tail of the low work function patch ThEED overlapping the high work function patch ThEED. This overlap pushes the ThEED peak separation distance closer together than the actual work function patch difference.

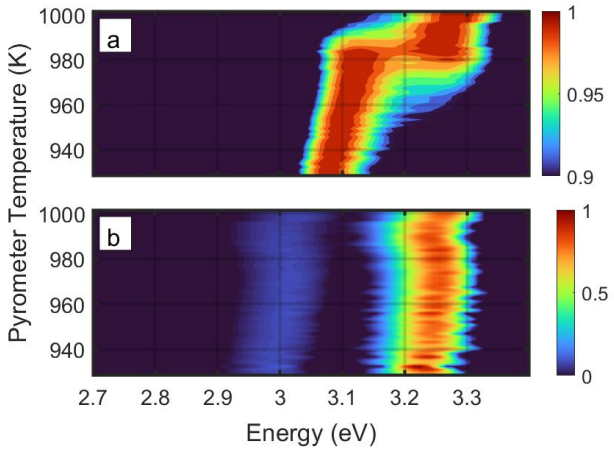

Figure 9: (a) Measured normalized ThEED curve intensities at various temperatures. (b) The normalized A_x distribution (the relative surface presence of each work function) for each temperature. For both contours, data across each temperature row is normalized with respect to its maximum value.

The data presented in Figure 9 reveals a subtle positive correlation between the extracted work function and temperature, suggesting an inherent temperature dependence of the work function. The observed results present a significant deviation from conventional methods that typically derive a singular work function value across a specified temperature range. This discrepancy highlights the potential limitations of assuming a temperature-independent work function in the analyzed system. Additionally, this positive trend could be used to estimate carrier concentration of the emission site, assuming the C12A7:e- is effectively an n-type semiconductor and the filled cage states act as donors. In an n-type semiconductor, as temperature increases the Fermi level drifts towards the mid-gap, especially for lightly doped cases. If we assume this the main factor for the temperature dependent work function, then we have $\varphi = (\varphi - E_c) - k_B T \ln\left(\frac{n}{N_c}\right)$, where E_c is the energy at the bottom of the conduction band, n is the carrier concentration, and N_c is the effective density of states approximated to be 2.26×10^{20} cm^{-3} assuming an electron effective mass of 1.3 from averaged measurements in [32]. The temperature derivative of the preceding equation yields :

$$\frac{d\varphi}{dT} = -k_B \ln\left(\frac{n}{N_c}\right) \rightarrow n = N_c e^{-\frac{1}{k_B}\frac{d\varphi}{dT}}, \quad (5)$$

Indicating carrier concentration n can be approximated using the slope of the extracted work function peak against temperature in the bottom contour of Figure 9. A linear fit between 930 and 980 K yield $\frac{d\varphi}{dT}/k_B = 9.54$ and 11.5 for the low and high work function presences, respectively. This yields a respective approximate carrier concentration of $n = 1.63 \times 10^{16}$ cm^{-3} and 2.29×10^{15} cm^{-3} for the two distinct work functions at the measured emission site. This approximate carrier concentration is below the theoretical maximum concentration of 2.33 x 10^{21} cm^{-3} [33] if every possible cage was in the complete electride state. This indicates electron current density could be improved further by enhancing this carrier concentration.

Figure 10a averages all the different temperature measurements into one work function presence curve, showing mostly consistent results across all temperatures measured. Although some spread in values is expected as work function is not constant with temperature, measurement noise can cause spread in extracted values, and slightly different convergence values of the steepest descent algorithm can increase error further. However, this variation is only minimally contributed to varying initial parameters of the steepest descent algorithm. Figure 10b shows the mean extracted work functions of 100 randomized initial parameters of A_x in Eq. (3) from only the ThEED taken at 1002 K. The error bars in both curves in Figure 10 represent a 95% confidence interval. The small magnitude of the error bars in Figure 10b provides strong evidence for the reliability and robustness of the observed trend in the extracted work functions.

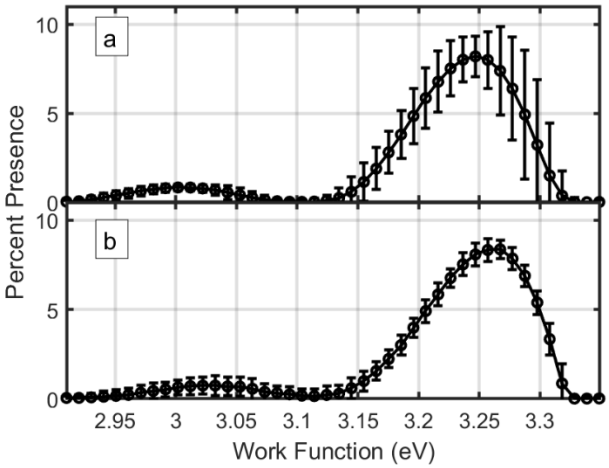

Figure 10: Mean relative work function presence extracted from ThEEDs using the steepest descent algorithm outlined in Figure 4. Error bars represent a 95% confidence interval. (a) Average extracted work values across all temperatures. (b) Average extracted work values at $T = 1002K$ using randomized initial values of A_x over 100 iterations.

Figure 11 shows a more traditional work function extraction method using a Richardson-Laue-Dushman (RLD) plot, giving a singular work function value. This plot exhibits a linear trend for thermal emission data, where the slope is correlated to the emitter work function. This is applied to both the experimentally measured and simulated ThEEDs. An RLD plot can be created starting with [34,35]

$$J = A^* T^2 exp\left[-\frac{\phi}{k_B T}\right], \tag{6}$$

where $A^* \equiv z_S k_B^2 \approx 1.201732 \times 10^6 \ \frac{A}{m^2 K^2}$ is the Richardson constant which is derived from fundamental physical constants assuming a free-electron model of the metal. This formula assumes only a singular work function is present, and the Richardson constant essentially represents the maximum possible electron current density that can be emitted thermally from a surface *per unit area, per unit of the square of temperature*, assuming an ideal free-electron gas model and a perfect surface. This universal constant A^* is distinct from the parameter A_x introduced in this work. Algebraic rearrangement of this equation yields:

$$Y = ln\left(\frac{J}{T^2}\right) = ln(A^*) + \left[-\frac{\phi}{k_B T}\right]. \tag{7}$$

For thermal emission, this relationship is anticipated to exhibit a linear dependence on the inverse temperature. It is important to note that the work function extracted from an RLD plot will be best represented in that measured temperature range, as work function can change with temperature. Analysis of the slope of this linear fit facilitates the elimination of the pre-exponential factor A^*,

$$\frac{\partial Y}{\partial T^{-1}} = \left[-\frac{\phi}{k_B}\right] \rightarrow \phi = -k_B \frac{\partial Y}{\partial T^{-1}}. \tag{8}$$

The electron emission current density J (a positive magnitude) for the measured data is $J = \int_{-\infty}^{\infty} \mathrm{j}_{obs}(E)\, dE$. Since $j_{obs}(E)$ is taken in discrete energy steps, this integral can be well approximated with trapezoidal integration. For simulated electron current density, each ϕ_x and A_x value from Figure 10 is inserted into Eq. (3) to find $\mathrm{j}_{sum}(E)$, followed by integrating $\int \mathrm{j}_{sum}(E) dE$ also with trapezoidal integration. This method extracts a work function of 3.12 eV and 3.08 eV for the experimentally measured and simulated ThEEDs, respectively. There is a vertical offset between simulation and experiment, however this does not impact work function as the slopes of these curves are of interest. These extracted work functions fit well, in between the two peaks of the predicted work function distributions as shown in Figure 9 and Figure 10.

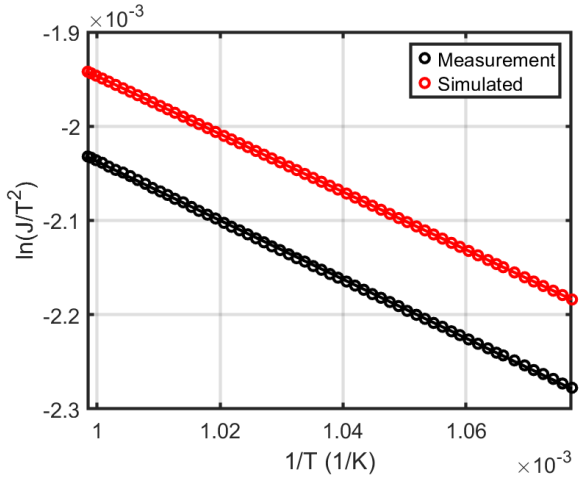

Figure 11: Richardson–Laue–Dushman plot to extract work function from experimental and simulated data via a linear fit. Work function of 3.12 eV and 3.08 eV extracted for measured and simulated data, respectively, with a coefficient of determination $r^2 > 0.999$.

Though this ThEED work function extraction method is shown to be mathematically accurate, it must be shown that it is also physically correct. This validation is done in two ways: the method predicts a known work function surface using 1) a Monte Carlo algorithm, and 2) experimental data.

A Monte Carlo (MC) algorithm is used to simulate a ThEED from experimentally measured work function maps on the C12A7:e^- surface. This allows a direct comparison between a surface of known work functions to the work functions predicted by the steepest descent algorithm. The MC algorithm selects a random location on the work function map, then generates an electron of a random energy following Fermi-Dirac statistics. This algorithm uses the Sommerfeld model to approximate the band structure from the C12A7:e^- emitter. If the electron energy in the surface normal direction is greater than the work function at that location, it emits. This is repeated until 10^6 electrons are emitted. Then, the ThEED can be observed as a histogram of the emitted electron normal or total energies to represent the NED or TED. Simulating 10^6 electrons was found to be an optimal tradeoff between computational time and a smoothly varying ThEED result. More simulated electrons will result in a near identical ThEED and less electrons will generate a ThEED distribution with more noise.

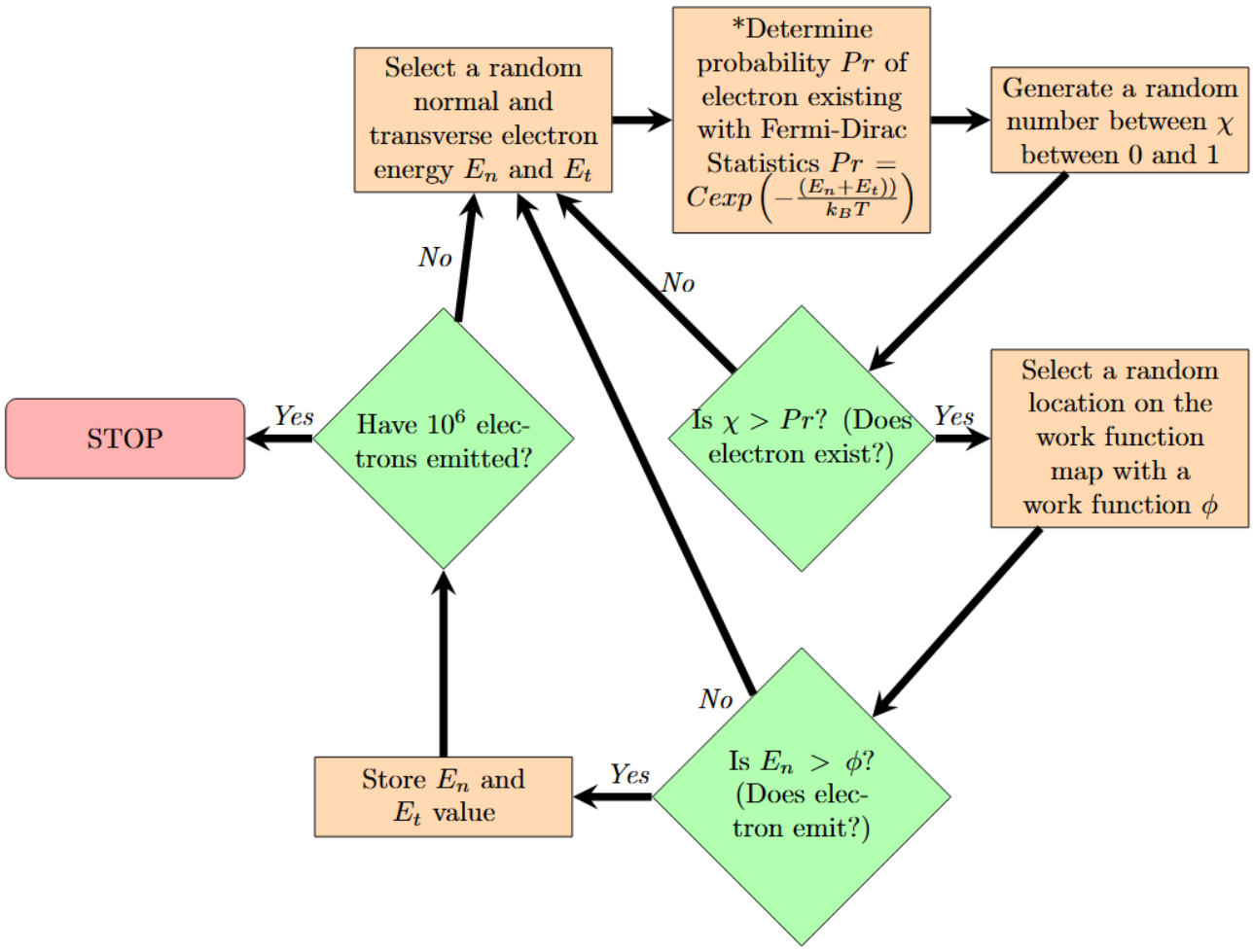

*Figure 12: Flow chart for the Monte Carlo algorithm to determine ThEED. *The parameter C is a normalization constant $C = exp(\varphi_{min}/k_BT)$ where φ_{min} is the minimum work function on the surface. Normalizing the Fermi-Dirac statistics and setting the minimum possible generated value of E_n to φ_{min} greatly enhance simulation speed.*

Figure 13a shows a measured work function map across two different locations on the C12A7:e^- surface taken via PEEM. The analysis area was selected to be approximately the same size as the ThEED analysis area. The C12A7:e^- surface was observed to consist of many different work functions, and even small work function variations within those regions. The MC algorithm was applied to both work function maps to determine their corresponding ThEEDs at 1000 K. Figure 13b shows a histogram of the corresponding work function map. Emission is dominated by patches with a low work function, as those with high work functions contribute negligibly. The emission origin work function, highlighted in green, therefore identifies the active patches responsible for the emitted electrons. This explains a ThEED analysis method's inability to account for high work function patches, as their emission is too insignificant to register. Both a NED and TED were determined to show the steepest descent algorithm can handle either a normal or total energy detector by using the correct formula in Eq. (1). The ThEEDs, shown in Figure 13c, were convolved with $IRF(\Delta E)$ to emulate detector smearing then fed into the

steepest descent algorithm to approximate the work function presence. Figure 14 shows the measured work function distribution compared to the work function distribution extracted with the steepest descent algorithm. These distributions are in excellent agreement at low energies work functions, validating the work function extraction method to have physical accuracy. However, the high energy work function patches were not found by the steepest descent algorithm, as these contribute negligibly to thermal emission.

Figure 13 and Figure 14 clearly demonstrate that polycrystalline C12A7:e^- exhibits spatially varying work functions. X-ray diffraction analysis confirmed the phase purity of these samples [8]. While previous studies indicated the potential presence of minor amounts of insulating calcium mono- and tri-aluminate phases (C3A and CA), these phases are unlikely to contribute to the observed work function variations. Due to their insulating nature, C3A and CA phases are not expected to be significant electron emitters. A more plausible explanation for the spatial distribution of work function is related to the stabilization of the Mayenite structure, $[Ca_{24}Al_{28}O_{64}]^{4+}(O^{2-})_2$, and the formation of the $[Ca_{24}Al_{28}O_{64}]^{4+}(4e\text{-})$ electride framework, primarily achieved through anionic substitution. Given the sensitivity of the processing route used to stabilize the cage structure via carbon C^{2-} ion templating within the $[Ca_{24}Al_{28}O_{64}]^{4+}$ framework [7], we propose that the observed work function variations arise from spatially heterogeneous C^{2-} ion templating within the Mayenite structure. Specifically, differing degrees of C^{2-} ion templating across the microstructure lead to variations in the work function.

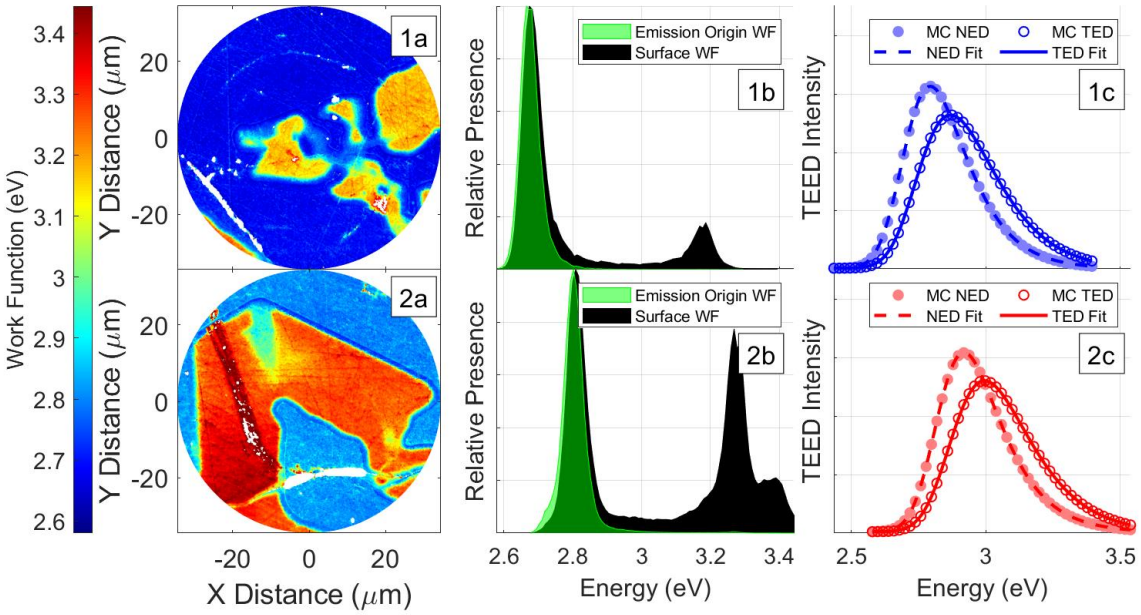

Figure 13: Measured work function maps (a) taken via PEEM at two arbitrary locations on the sample surface labelled 1 and 2. (b) Work function histogram of corresponding work function map in black. Histogram of the work function origin of emitted electrons in the MC simulation in green. (c) ThEEDs simulated with the MC simulation and then fit with the work function extraction method are presented as circles and curves, respectively. Both the NED and TED are shown with

filled and open circles, respectively. All ThEEDs are broadened using the $IRF(\Delta E)$ distribution shown in Figure 7 prior to extracting work functions.

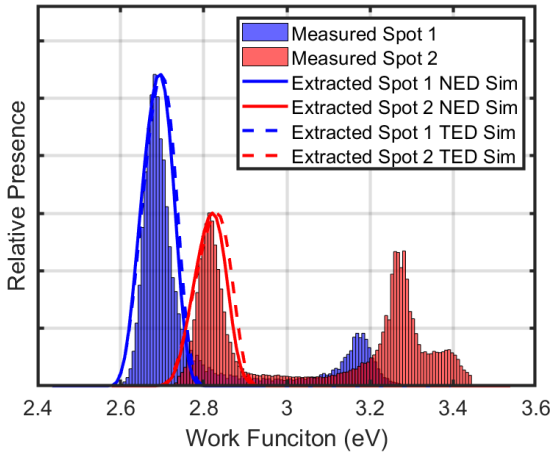

Figure 14: Comparison of measured and extracted work function distributions. A MC algorithm predicted ThEEDs from the measured work function distribution, then a steepest descent algorithm extracted a predicted work function distribution from the ThEEDs. The solid and dashed lines represent the MC algorithm determining normal and total energy ThEEDs, respectively. Excellent work function distribution agreement exists regardless of normal or total energy MC simulations.

PEEM measurements. Additional measurements were carried out on a commercial spectrometric low energy electron microscope SPELEEM (photoemission electron-, resp. low energy electron microscope PEEM/LEEM III Elmitec GmbH) equipped with an energy filtering analyzer (hemispherical energy analyzer, energy resolution 125 meV). The energy resolution of the analyzer is determined by measuring the full width at half maximum (FWHM) of the elastic peak of the electron beam produced by the instrument's electron source. The PEEM/LEEM microscope is equipped with a Schottky field emission gun Schottky (FEG), with an energy spread in the range [350, 700 meV] [36]. The kinetic energy distribution of the FEG electron beam can be imaged in the dispersive plane of the analyzer. The signal obtained corresponds to the convolution product of the source and the analyzer's response function. If assumed Gaussian contributions, the squares of the signal FWHMs sum up. The measured experimental FWHM of the electron elastic peak is 370 meV. Considering the minimum energy spread of the electron source 350 meV (worst case), the determined energy resolution of the hemispherical analyzer is 120 meV: $370^2 - 350^2 = 120^2$.

Base pressure in the UHV instrument is in the 10^{-10} mbar range. Measurements of C12A7:e^- work function were carried out using two independent methods. First, one makes use of the low energy electron imaging mode [37,38]. In a LEEM microscope, the sample surface is illuminated by a collimated beam of electrons, whose landing kinetic energy E_0 can be adjusted by biasing the sample with respect to the electron gun with a potential called the start voltage (SV). Depending on the start voltage value, the incoming electrons are either reflected before they

reach the surface (E_0 < 0 eV, mirror electron imaging mode MEM) or scattered from it (E_0 > 0 eV, low energy electron imaging mode LEEM). The transition between these two imaging modes (MEM vs. LEEM) is accompanied by a sharp drop in electron surface reflectivity for a start voltage value characteristic of the work function difference between the electron gun material and the surface sample. The work function of the surface is mapped by determining the SV transition onset at any point in the image. The electron reflectivity drop of the LEEM-IV curves has been modeled by a complementary error function (erfc), and the onset voltage is taken at the erfc center [13,39]. The absolute value of the sample surface work function is obtained by mapping the work function of a reference material. The reference adopted in this work is that of a highly oriented pyrolytic graphite (HOPG) taken at 4.58 eV [40]. In addition, it is also possible to extract the work function (without using a reference sample) from measurements of the total electron energy distribution TED in spectrometric photoemission mode. The value of the work function is related to those of the photon energy and the width of the TED function by the relation $\varphi = h\nu - TED_{Width}$. The energy of the photon is $h\nu = 4.88\ eV$ ($254\ nm$, UV Source Energetiq LDLS EQ-77, UV Semrock filter Hg01 - 254 - 25). The TED width is obtained by extrapolating the tangents of the kinetic energy profile at 1.5% of the maximum of the photoemission peak. The methods used to prepare the Mayenite surface are identical to those described above.

A ThEED curve at 1021 K was collected at a known location on a sample shown by both low-energy electron microscopy LEEM and thermal electron emission microscopy ThEEM, see Figure 15. This ThEED incorporated simultaneous emission from three known work function patches measured at 2.47, 2.63, and 2.76 eV. The different patches are labelled A, B, C in figure 15. A separate thermal emission measurement was performed on each patch individually, and an RLD slope fit was used to determine each work function. They exhibit work function values lower than what is shown in the ThEED measurements using the setup shown in Figure 1. This is due to a higher extraction voltage of 18 kV overcoming low work function patch fields (external ES field $F_{ext} > 5 \times 10^6$ V/m). This high extraction voltage results in a large solid acceptance angle of the immersion objective lens, and the acquired electron distributions correspond to the ThEEDs of total electron energies TED [12], see the appendix for more details.

Figure 16 shows an extracted work function distribution using the steepest decent method from the ThEED originating from the spot marked in Figure 15(b). Three distinct work function regimes emerged naturally in the extraction; each highlighted a unique color. The peaks of each of these three regimes match excellently to the known work function values of each patch extracting 2.47 (2.47 eV measured via RLD slope), 2.63 (2.63), and 2.85 (2.76) eV. The areas of each shaded regime allow us to estimate the relative areal concentration of each work function patch in the analysis area with 17%, 28%, and 55% concentrations for the low, medium, and high work functions patch, respectively. This notably differs from the expected nearly equal concentration of all three patches. The work function extraction method loses accuracy of relative intensity for higher work functions, as large changes to A_x only minimally impact the ThEED due to domination of low work function emission. This can lead to inaccuracies in the areal concentration patch fit for larger work functions.

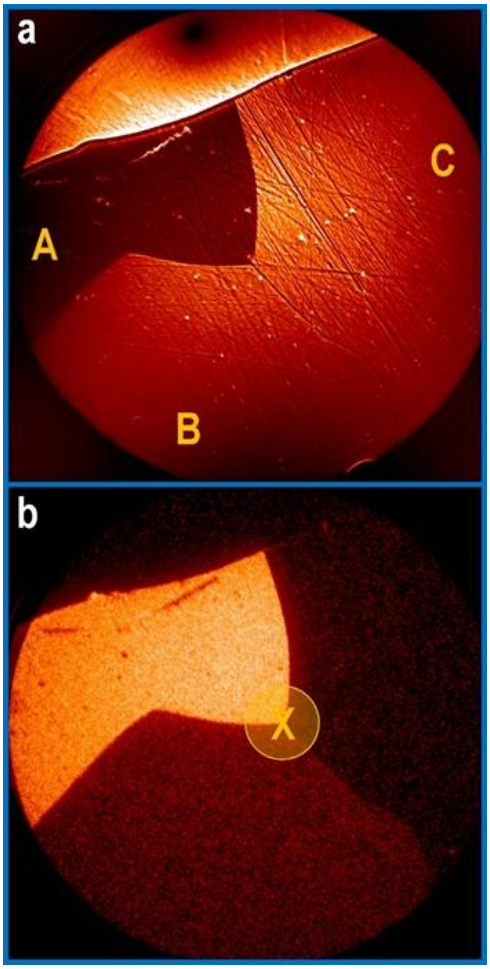

Figure 15: (a) LEEM image of Mayenite surface showing 3 distinct patches (A, B, C) of unique work function. (b) ThEEM image of same location, where low work function patch dominates electron emission. Location marked on (b) represent region where a ThEED was measured, capturing emission from all three patches simultaneously, temperature is 784 K. Field of view is 88 µm. External extracting ES field is 5250 kV/m. Linear (a), logarithmic (b) rendering histograms.

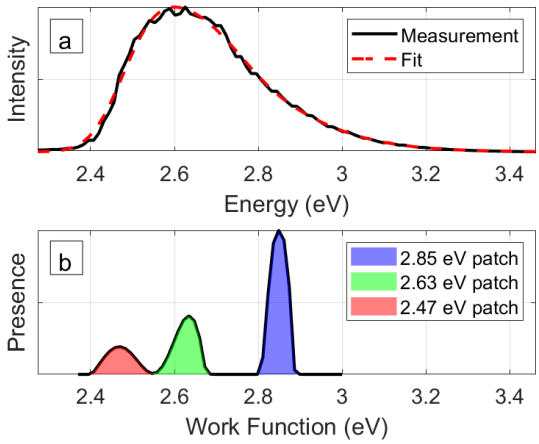

Figure 16: (a) ThEED measurement and fit from steepest descent algorithm represented by the solid and dashed curves, respectively. (b) Extracted work functions from ThEED measured at the location marked in Figure 15b. The three peaks are each shaded and the two lower work function patches that dominate emission are in excellent agreement with the measured distinct work function patch values.

Conclusion

Heterogenous surfaces contain thermal emission information that is too complex to be modelled properly with standard Richardson-Laue-Dushman methods. Surface characterization techniques such as Photoemission Electron Microscopy work function mapping and/or electron backscatter diffraction have been used to model a heterogenous surface and then predict thermal emission electron current. This work successfully demonstrates a new approach utilizing a steepest-descent algorithm to predict work function distributions on heterogenous surfaces using only measured Thermally Emitted Electron Distribution data. This circumvents the potential need for additional surface characterization. Additionally, this method allows for the predicted work function distribution to take place exactly where the ThEED measurement is performed, removing any uncertainty on measurement location matching across different characterization techniques.

This work function extract methodology was demonstrated on a low work function C12A7:e^- sample, which was shown to have a heterogenous surface consisting of many varying work functions. The method was further validated with comparisons against Thermally Emitted Electron Distribution data taken at a known characterized surface location, as well as validation through a Monte Carlo algorithm to predict Thermally Emitted Electron Distribution curves from measured Photoemission Electron Microscopy work function maps.

A future improvement of this work function extract method would be to couple it with a temperature extraction at the analysis location without relying on a temperature measurement. Thermocouples do not represent a sample surface temperature well, and pyrometers can suffer from incorrect emissivity values and positioning on the sample surface. Heated samples may have

a non-uniform temperature across a broad area causing discrepancies with the pyrometer and analysis area temperature. Extracting the temperature from ThEEDs would instill more confidence in the temperature at the specific analysis location. Additionally, this methodology could be extended beyond that of thermal emission and predict work function distributions of field emitters.

Acknowledgements

This research for T. C. Back was supported by the Air Force Office of Scientific Research under Project No. FA9550-20RXCOR027. J. Ludwick was supported by the Air Force Research Labs under contract No. FA8650-16-D-5408. G. Saïz and L. Douillard were supported by the Air Force Research Labs under contract No. FA8655-23-1-7073.

Appendix I: Image Formation in an Electron Microscope

In an emission electron microscope, electrons are accelerated by a uniform electric field aligned on the optical axis of the instrument (normal axis) $\hat{z}$. In the following, the notations are those of [12]. Let us consider a conductive specimen, whose flat surface is perpendicular to the instrument axis. The $\hat{z}$ and $\hat{r}$ directions denote, respectively, the normal and the radial directions. The movements of the electrons are restricted to the ($\hat{z}$, $\hat{r}$) plane, z_0 ($z_0 < 0$) is the location of the electron emitting point and z_a ($z_a = 0$) is the location of the anode objective lens.

Electrons are emitted from the specimen at position (z_0, r_0) with an initial velocity $\overrightarrow{v_0} = (\dot{z_0}, \dot{r_0})$, this velocity vector defines an angle α_0 with the normal axis (*i.e.,* α_0 is the electron take-off angle relative to the $\hat{z}$ axis). These electrons are accelerated in the ($\hat{z}$, $\hat{r}$) plane along parabolic trajectories. Here, the action of the diverging field in the close vicinity of the objective aperture is neglected [12]. At the position of the anode $z_a = 0$, the accelerating action of the electric field ceases and the velocity vector $\overrightarrow{v_a} = (\dot{z_a}, \dot{r_a})$ defines a final angle α^* relative to the optical axis. The angle α^* is given by $\sin(\alpha^*) = \frac{\dot{r_a}}{v_a}$. Only the electron normal velocity component is modified along the trajectory; the radial velocity component is unaffected by the electric field, $\dot{r_a} = \dot{r_0} = v_0 \sin(\alpha_0)$. The initial and final angles are thus linked by the relationship $\sin(\alpha^*) = \frac{v_0}{v_a}\sin(\alpha_0)$. The electron velocities are defined by the kinetic energies $\frac{1}{2}mv_0^2 = E_0$ and $\frac{1}{2}mv_a^2 = E_0 + eU$, where E_0 is the kinetic energy of the electrons at the point of emission, U is the acceleration voltage between the specimen and the anode and m the electron mass. Ultimately, we obtain:

$$\sin(\alpha^*) = \sqrt{\frac{E_0}{E_0 + eU}}\sin(\alpha_0)$$

In a LEEM / PEEM microscope, an aperture (*contrast aperture*) can be introduced in the imaging column at the entrance of the electron analyzer (in a plane conjugated with the focal plane of the objective lens), where post acceleration angles α^* are well defined (in-plane $k_{||}$ momentum

vectors plane). This contrast aperture defines the range of acceptance angles α^*. A classical value for α^* is 20 mrad = 1.145° (half-cone angle). Accelerating voltage U is in the range [15000 V, 20000 V].

Numerical Application with E_0 = 3 eV, U = 20000 V, α^* = ± 20 mrad gives $\alpha_0 = \pm \frac{\pi}{2} = \pm 90°$. So, the high extraction voltage results in a large solid acceptance angle of the immersion objective lens, and the acquired electron distributions correspond to the total electron energies TED (at low kinetic energies).

For the ARGUS CU used for ThEED measurements, illustrated in Figure 1, the acceptance angle of the analyzer is ±3.8° (α^* = 66.3 mrad). The accelerating voltage in the experiment was U = 300 V. Assuming, E_0 = 3 eV, this system captures initial launch angles of $\alpha_0 = \pm 41.76°$, failing to capture all angles of emitted electrons. However, in the context of thermal emission from a flat surface, this system observes a TED.

Assuming a work function and temperature of $\phi = 3\ eV$ and $T = 1000\ K$, respectively, j_{tot} in Eq. (1) can be repurposed as a probability distribution of electrons emitting (p_{emit}) between $E_0 = \phi$ to ∞ with

$$p_{emit}(\mathrm{T}, E_0) = \mathrm{A}(E_0 - \phi) \exp\left(-\frac{E_0}{k_B T}\right) H(E_0 - \phi),$$

where $A = 1.773 \times 10^{17}$ eV^{-2} is a normalization constant to ensure integrating p_{emit} from $E_0 = \phi$ to ∞ yields a probability of 1. Assuming the emitted electron has the smallest possible normal energy component of 3 eV ($z_0 = 1.03 \times 10^6\ m/s$), then the smallest possible initial transverse energy to achieve $\alpha^* \geq 3.8°$ is 1.34 eV ($r_0 = 6.86 \times 10^5\ m/s$) with a launch angle $\alpha_0 = 33.7°$. This yields a total energy of $E_0 = 4.34\ eV$ to satisfy $\alpha^* \geq 3.8°$. The probability of such an electron emitting, found by integrating $\int_{4.34\ eV}^{\infty} p_{emit}(\mathrm{T}, E_0) dE_0$ is 2.922×10^{-6}, effectively a negligible portion of emission. Increasing the assumed normal energy of the emitted electron would decrease this probability further. Thus, the observed spectrum is effectively a TED.

Appendix II: Used Notations

Quantity	**Unit**	**Symbol**
Electron-current density per unit energy range	A·m^{-2}·eV^{-1}	j
Theoretical electron-current density per unit *normal* energy range for a *single emitting work function*	A·m^{-2}·eV^{-1}	j_n
Theoretical electron-current density per unit *total* (normal + transverse) energy range for a *single emitting work function*	A·m^{-2}·eV^{-1}	j_{tot}
Theoretical electron-current density per unit energy range for *multiple emitting work functions (assume total energy in this work)*	A·m^{-2}·eV^{-1}	j_{sum}
Measured electron-current density per unit energy range *(assume total energy in this work)*	A·m^{-2}·eV^{-1}	j_{obs}
Electron-current density	A·m^{-2}	J

Sommerfeld electron supply constant: electron-current density per unit area of energy space	$A \cdot m^{-2} \cdot eV^{-2}$	z_S

Author Declarations

Conflict of Interest

The authors have no conflicts to disclose.

Data Availability

The data that support the findings of this study are available from the corresponding author upon reasonable request.

Bibliography

1. O. W. Richardson, Phys. Rev. **23**, 153 (1924).
2. S. Dushman, Rev. Mod. Phys. **2**, 381 (1930).
3. C. Herring and M. H. Nichols, Rev. Mod. Phys. **21**, 185 (1949).
4. D. Chen, Modeling Nonuniform Thermionic Emission from Heterogeneous Cathodes, University of Wisconsin-Madison, 2022.
5. D. Chen, R. Jacobs, J. Petillo, V. Vlahos, K. L. Jensen, D. Morgan, and J. Booske, Phys. Rev. Appl. **18**, 054010 (2022).
6. S. W. Kim and H. Hosono, Philos. Mag. **92**, 2596 (2012).
7. J. Mackey, T. Back, M. Berger, and A. Sayir, J. Am. Ceram. Soc. **104**, 2238 (2021).
8. A. Sayir, M. Berger, T. C. Back, and J. Mackey, J. Am. Ceram. Soc. **104**, 5750 (2021).
9. L. P. Rand and J. D. Williams, IEEE Trans. Plasma Sci. **43**, 190 (2015).
10. Y. Huang, X. Wang, G. Cui, P. Wang, and D. Cai, Aerospace **10**, 339 (2023).
11. A. Post, J. F. Plaza, J. Toledo, D. Zschätzsch, M. Reitemeyer, L. Chen, A. Gurciullo, A. Siegel, P. J. Klar, P. Lascombes, and B. Seifert, IOP Conf. Ser. Mater. Sci. Eng. **1226**, 012092 (2022).
12. G. F. Rempfer, K. K. Nadakavukaren, and O. H. Griffith, Ultramicroscopy **5**, 437 (1980).
13. C. Mathieu, N. Barrett, J. Rault, Y. Y. Mi, B. Zhang, W. A. de Heer, C. Berger, E. H. Conrad, and O. Renault, Phys. Rev. B **83**, (2011).
14. M. Escher, K. Winkler, O. Renault, and N. Barrett, J. Electron Spectrosc. Relat. Phenom. **178–179**, 303 (2010).
15. J. Rault, Structure Chimique et Électronique Des Interfaces Métal/Ferroélectrique En Fonction de La Polarisation Ferroélectrique, Université Pierre et Marie Curie, 2013.
16. J. W. Gadzuk and E. W. Plummer, Rev Mod Phys **45**, 487 (1973).
17. E. L. Murphy and R. H. Good, Phys. Rev. **102**, 1464 (1956).
18. R. H. Fowler and L. Nordheim, Proc R Soc Lond A **119**, 173 (1928).
19. R. D. Young, Phys. Rev. **113**, 110 (1959).
20. L. B. Lucy, Astron. J. **79**, 745 (1974).
21. W. H. Richardson, J. Opt. Soc. Am. **62**, 55 (1972).

22. R. D. Young and C. E. Kuyatt, Rev. Sci. Instrum. **39**, 1477 (1968).
23. T. L. Westover, G. Powell, and T. S. Fisher, in *ASMEJSME 2007 Therm. Eng. Heat Transf. Summer Conf. Vol. 2* (ASMEDC, Vancouver, British Columbia, Canada, 2007), pp. 493–498.
24. R. Reifenberger, H. A. Goldberg, and M. J. G. Lee, Surf. Sci. **83**, 599 (1979).
25. L. Lin, R. Jacobs, T. Ma, D. Chen, J. Booske, and D. Morgan, Phys. Rev. Appl. **19**, 037001 (2023).
26. R. Bachelet, F. Sánchez, F. J. Palomares, C. Ocal, and J. Fontcuberta, Appl. Phys. Lett. **95**, 141915 (2009).
27. Z. Zhang, P. Qian, X. Yang, B. Wu, H. L. Cai, F. M. Zhang, and X. S. Wu, Sci. Rep. **12**, 2499 (2022).
28. D. Wrana, C. Rodenbücher, W. Bełza, K. Szot, and F. Krok, Appl. Surf. Sci. **432**, 46 (2018).
29. D. Wrana, K. Cieślik, W. Belza, C. Rodenbücher, K. Szot, and F. Krok, Beilstein J. Nanotechnol. **10**, 1596 (2019).
30. T. J. Whittles, S. C. Parks, H. Wang, P. Jiang, Z. Zhong, P. A. van Aken, and J. Mannhart, Adv. Mater. Interfaces **11**, 2400109 (2024).
31. S. Phark and Y. J. Chang, Nanoscale Res. Lett. **10**, (2015).
32. S. W. Kim, R. Tarumi, H. Iwasaki, H. Ohta, M. Hirano, and H. Hosono, Phys. Rev. B **80**, 075201 (2009).
33. P. V. Sushko, A. L. Shluger, M. Hirano, and H. Hosono, J. Am. Chem. Soc. **129**, 942 (2007).
34. O. Richardson and A. Young, Proc. R. Soc. Lond. Ser. Contain. Pap. Math. Phys. Character **107**, 377 (1925).
35. S. Dushman, Phys. Rev. **21**, 623 (1923).
36. E. Bauer, *Surface Microscopy with Low Energy Electrons* (Springer New York, New York, NY, 2014).
37. C. Nakakura, M. Anderson, and G. Kellogg, *Imaging Doped Silicon Test Structures Using Low Energy Electron Microscopy.* (Sandia National Laboratories (SNL), Albuquerque, NM, and Livermore, CA (United States), 2010).
38. J. Jobst, L. M. Boers, C. Yin, J. Aarts, R. M. Tromp, and S. J. van der Molen, Ultramicroscopy **200**, 43 (2019).
39. A. L. Fernandes Cauduro, L. H. Hess, D. F. Ogletree, J. W. Schwede, and A. K. Schmid, Appl. Phys. Lett. **115**, (2019).
40. H. Kawano, Prog. Surf. Sci. **97**, 100583 (2022).